



Cite this: *Nanoscale*, 2015, 7, 9844

## Ultrarapid and ultrasensitive electrical detection of proteins in a three-dimensional biosensor with high capture efficiency†

Bo-Yeong Kim,<sup>a</sup> Il-yung Sohn,<sup>b</sup> Doowon Lee,<sup>b</sup> Gill Sang Han,<sup>b</sup> Won-Il Lee,<sup>c</sup> Hyun Suk Jung<sup>b</sup> and Nae-Eung Lee<sup>\*a,b,c</sup>

The realization of a high-throughput biosensor platform with ultrarapid detection of biomolecular interactions and an ultralow limit of detection in the femtomolar (fM) range or below has been retarded due to sluggish binding kinetics caused by the scarcity of probe molecules on the nanostructures and/or limited mass transport. Here, as a new method for the highly efficient capture of biomolecules at extremely low concentration, we tested a three-dimensional (3D) platform of a bioelectronic field-effect transistor (bio-FET) with vertically aligned and highly dense one-dimensional (1D) ZnO nanorods (NRs) as a sensing surface capped by an ultrathin TiO<sub>2</sub> layer for improved electrolytic stability on a chemical-vapor-deposited graphene (Gr) channel. The ultrarapid detection capability with a very fast response time (~1 min) at the fM level of proteins in the proposed 3D bio-FET is primarily attributed to the fast binding kinetics of the probe–target proteins due to the small diffusion length of the target molecules to reach the sensor surface and the substantial number of probe molecules available on the largely increased surface area of the vertical ZnO NRs. This new 3D electrical biosensor platform can be easily extended to other electrochemical nanobiosensors and has great potential for practical applications in miniaturized biosensor integrated systems.

Received 8th February 2015,  
Accepted 21st April 2015

DOI: 10.1039/c5nr00909j

www.rsc.org/nanoscale

## Introduction

Extensive research effort has been made to develop fast, highly sensitive, and miniaturized biosensors for point-of-care diagnostics.<sup>1–5</sup> In particular, the use of nanostructured materials in electrochemical<sup>6–16</sup> and gravimetric biosensors<sup>17</sup> has attracted great attention due to the possibility of obtaining high sensitivity, low limit of detection (LOD), and real-time and label-free detection, because nanostructured materials show extremely high sensitivity to bimolecular interactions. The detection of extremely dilute target molecules at the femtomolar (fM) level or below is of great interest for clinical diagnostics of diseases with low concentration biomarkers and for the detection of secreted biomolecules from a single cell.<sup>14,17–19</sup> However, the development of these high-through-

put nanobiosensor platforms with ultralow LODs at the fM level or below and with high sensitivity and ultrarapid detection (within a minute) of biomolecular interactions has not been achieved because the binding kinetics of probe–target molecules are limited by the small number of probe molecules on the small surface of the nanostructures and/or limited mass transport to the sensor's surface.<sup>1</sup> To achieve ultrarapid and ultrasensitive detection in the minute range at target concentrations at the fM level, it is essential to develop engineered probe molecules with high affinity and selectivity, to increase the immobilized density of probe molecules in a given sensor area and/or to optimize the sensor geometry to increase mass transport for fast binding kinetics of target molecules with probe molecules.<sup>1,17,20–22</sup>

The binding kinetics of the probes and target molecules on nanosensors or microsensors in lateral flow systems is generally described by the Damköhler number,  $D_a$ , which is the ratio of reactive to diffusive flux.<sup>1,17</sup> The Damköhler number can be expressed as  $D_a = k_{on}b_mA_s/(J_D/C_o)$ , where  $k_{on}$  is the rate of association,  $b_m$  is the surface density of probe molecules on the sensor surface,  $A_s$  is the surface area of the sensor (here, ZnO nanorods (NRs)),  $J_D$  is the collection rate of target molecules reaching the sensor surface, and  $C_o$  is the concentration of target molecules.<sup>1,17</sup> For  $D_a \gg 1$ , the binding kinetics are

<sup>a</sup>SKKU Advanced Institute of Nanotechnology (SAINT), Sungkyunkwan University, Suwon, Gyeonggi-do 440-746, South Korea

<sup>b</sup>Department of Advanced Materials Science & Engineering, Sungkyunkwan University, Suwon, Gyeonggi-do 440-746, South Korea

<sup>c</sup>Samsung Advanced Institute for Health Sciences and Technology (SAIHST), Sungkyunkwan University, Suwon, Gyeonggi-do 440-746, South Korea.

E-mail: nelee@skku.edu

†Electronic supplementary information (ESI) available. See DOI: 10.1039/c5nr00909j



entirely mass-transport limited, while for  $D_a \ll 1$ , the kinetics of capture become reaction limited. Experimentally, one-dimensional (1D) bioelectronic field-effect transistors (bio-FETs) based on a single Si nanowire (NW) showed ultrasensitive detection of proteins and deoxyribonucleic acids (DNAs) down to concentrations in the fM range and with response times of several tens of minutes.<sup>23–25</sup> However, other experiments and numerical considerations on the protein binding kinetics on Si NW bio-FETs showed contradictory results with response times of several tens of minutes at pM levels or above.<sup>17,20,26,27</sup> For example, numerical simulations on 1D NW nanosensors in the microfluidic channel indicated that the binding kinetics are reaction limited.<sup>1</sup> It may take several days for one target molecule to be attached to the single NW surface at the fM level because binding events of the target and probe molecules rarely happen at extremely low  $C_0$  due to the scarcity of probe molecules on the small area of Si NW giving a very small  $b_m A_s$  value.<sup>1</sup> A lack of saturation in the sensing signal in 1D nanobiosensors can limit the LOD during detection of protein–protein interactions. To expedite the detection speed with fast binding kinetics at extremely low  $C_0$  therefore, it is important to develop new approaches to simultaneously increase the  $b_m A_s$  value and the diffusion flux,  $J_D$ , simultaneously.<sup>20</sup>

Bio-FETs based on a two-dimensional (2D) nanomaterial channel with a microscale sensing area are capable of achieving ultrarapid detection of biomolecular interactions due to their relatively large  $b_m A_s$  values; they have a larger number of probe molecules on the sensing channel. In this sense, 2D bio-FETs based on graphene (Gr),<sup>9,11,12,28,29</sup> reduced graphene oxide (rGO)<sup>30,31</sup> and MoS<sub>2</sub><sup>32,33</sup> have potential as biosensors for the rapid detection of protein and DNA interactions. For example, a 2D bio-FET based on a large area rGO channel showed a response time of about 12 minutes for the detection of the prostate specific antigen/1-antichymotrypsin (PSA–ACT) complex, a protein biomarker for prostate cancer, at the 1 fM level.<sup>30</sup>

Even though there is still room for improvement in the detection speed of extremely dilute target molecules, there have been no such efforts for the development of bio-FETs having the capability of achieving ultrarapid detection with response time near one minute. As a new method, three-dimensional (3D) channel structures with vertical, highly dense 1D NWs or NRs on a microscale channel in bio-FETs are interesting because the surface area of the channels can be increased dramatically for the functionalization of a large number of probe molecules in a given device area, and the diffusion distance of probe molecules to reach the probe-functionalized surface of the vertical 1D nanostructures can be reduced to the nanoscale level for effective mass transport. However, to our knowledge, there have been no such studies on immunosensing using bio-FETs with 3D channel structures.

Herein, we demonstrate a 3D bio-FET with vertical, highly dense ZnO NR sensing materials on a chemical vapor-deposited (CVD) Gr channel which is an excellent substrate for

directional growth of ZnO NRs and their ambipolar characteristics enable one to extract the sensing parameters more clearly. Furthermore, the conductance of the CVD Gr channel can be easily modulated by the electrical responses from biomolecular interactions on the surface of the ZnO NRs because of the high electrical coupling between Gr and ZnO NRs.<sup>34</sup> A 3D bio-FET with vertically grown ZnO NRs on a Gr channel was successfully fabricated with ambipolar characteristics. The fabricated 3D bio-FET was used to detect the target analytes of the PSA–ACT complex. We obtained a sensitivity of  $\sim 8$  mV dec<sup>-1</sup> from the charge neutrality point (CNP), a dynamic range of  $10^7$ , a LOD of  $100 \text{ fg ml}^{-1}$  ( $\sim 1$  fM), and a detection time of 64 s at a target concentration at the fM level. The 3D bio-FET showed significant improvements in sensitivity, dynamic range, and response time compared with other 1D or 2D bio-FETs.

## Results and discussion

A schematic illustration of a 3D channel bio-FET with vertically grown ZnO NRs on the CVD Gr of the SiO<sub>2</sub>/Si wafer and bio-functionalization with PSA–ACT complex probe molecules is shown in Fig. 1a and b. The channel length between the source and drain electrodes of the 3D channel FET was set at  $300 \mu\text{m}$  and the channel width was  $6000 \mu\text{m}$ . Details of the fabrication process of a 3D bio-FET (Fig. S1†) are explained in the Experimental section. The single layer graphene (SLG) on the SiO<sub>2</sub>/Si wafer as a transport channel was transferred using a gold (Au) transfer method previously developed by our group,

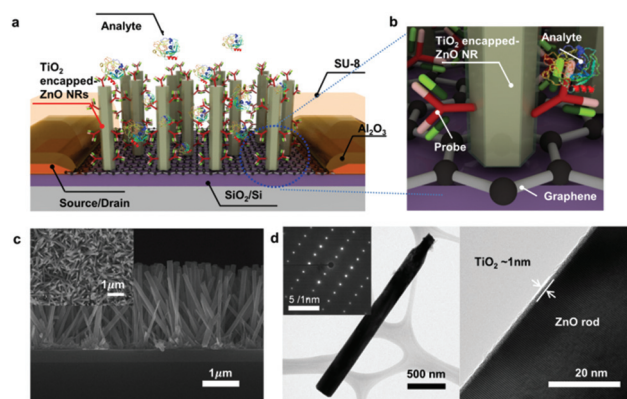


**Fig. 1** (a) Schematic illustration of a 3D channel FET biosensor. The ZnO NRs were vertically grown on the Gr channel area. The source/drain electrodes are electrically isolated from the analyte solution by passivation of a thin Al<sub>2</sub>O<sub>3</sub> layer and SU-8 pattern. (b) Schematic showing the immobilization of antibody probe molecules on the surface of TiO<sub>2</sub>-encapped ZnO NR. (c) Cross-sectional FE-SEM image of ZnO NRs grown on CVD Gr (inset: top view FE-SEM image). ZnO NRs approximately  $2.5 \mu\text{m}$  in length with a hexagonal shape were grown on Gr using a solution growth method. (d) Micrograph of a TiO<sub>2</sub>-encapped ZnO NR with the selected area diffraction pattern as an inset (left) and high-resolution image of the ultrathin TiO<sub>2</sub> layer capping the ZnO NR (right) obtained by transmission electron microscopy.



which provided an ultraclean surface for further surface functionalization and high electrical performance.<sup>29,35</sup> Growth of ZnO NRs on the Gr channel was achieved using a solution growth method.<sup>36–40</sup> Details of the SLG synthesis and transfer process are provided in the Experimental section. Cross-sectional and top-view images of the grown ZnO NRs obtained by field-emission scanning electron microscopy (FE-SEM) indicated the average height ( $H$ ) and diameter of ZnO NRs at  $\sim 2.5 \mu\text{m}$  and  $\sim 170 \text{ nm}$ , respectively (Fig. 1c). Assuming a uniform distribution of ZnO NRs on the channel area, the ratio of the total sensing surface area of ZnO NRs ( $A_s$ ) to the device channel area  $A_c$ ,  $A_s/A_c$ , was estimated to be  $\sim 23$ , which suggests a dramatic increase in the sensing area of 3D ZnO NRs compared to that of 2D Gr. Details of characterization of the CVD Gr and ZnO NRs are described in Fig. S2.† A further important feature of this fabrication method is the passivation of the source and drain electrodes using a photo-patternable SU-8 epoxy from the electrolyte to minimize the leakage current between the electrolyte and the electrodes and attachment of the probe molecules on the source–drain electrodes (see the details in the Experimental section). Due to the instability of ZnO NRs in aqueous environments,<sup>41</sup> the surface of ZnO NRs was also capped by an ultrathin  $\text{TiO}_2$  layer ( $\sim 1 \text{ nm}$ )<sup>42</sup> via atomic layer deposition (ALD) (Fig. S3†). The image of a  $\text{TiO}_2$ -encapped ZnO NR obtained by high-resolution transmission electron microscopy (Fig. 1d) confirmed the ultrathin  $\text{TiO}_2$  layer on the ZnO NR surface.

To understand the fundamental characteristics of solution-gated 3D channel FETs, their responses to solutions with different ionic concentrations were investigated. The transfer characteristics, the source–drain current ( $I_{\text{DS}}$ ) versus the gate bias voltage ( $V_{\text{G}}$ ), of 3D channel FETs and Gr FETs measured in sodium phosphate buffer solutions with various ionic concentrations at a fixed pH 7.4 are shown in Fig. S4a and S4b,† respectively. Interestingly, the 3D channel FET showed excellent ambipolar transfer characteristics similar to those of Gr FET. For both 3D and 2D Gr channel FETs, the transfer curve shifted to a more negative voltage when the ionic concentration of the buffer solutions was increased, and changes in the conductivity and CNP occurred at the same time.<sup>43</sup> The electrical double layer (EDL) thickness decreased when the ionic concentration increased, accompanied by an increase of the EDL capacitance value, resulting in a reduced surface potential and, in turn, a shift of the charge neutrality point (CNP) in the negative direction.<sup>44</sup> Similar behaviors were reported for electrolyte-gated SLG FETs, which were explained by electrostatic gating effects.<sup>43,45–47</sup> The sensitivity of the 3D channel FET to ionic concentration was notably higher than that of Gr FET (Fig. S4c†). The increased responsivity of the 3D channel FET to ionic strength is attributed to the increased surface area of the 3D channel due to the high density, high aspect-ratio ZnO NRs on the Gr layer.

In bio-FETs used for immunosensing, having a high density of probe proteins on the channel surface is critical for enhancing the sensitivity, LOD, and dynamic range. Details of the immobilization procedure are described in Fig. S5.† To

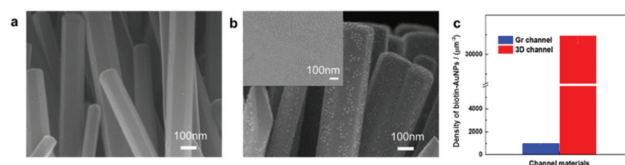


**Fig. 2** The FE-SEM images were observed to confirm the binding of gold nanoparticles conjugated with biotin (biotin-AuNPs) and streptavidin functionalized on the  $\text{TiO}_2$  surface: (a) before and (b) after  $\text{O}_2$  plasma treatment of  $\text{TiO}_2/\text{ZnO}$  NRs, respectively. The inset in Fig. 4b was obtained after binding of biotin-AuNPs with streptavidin functionalized on the Gr surface using PBSE linker molecules. (c) The density of biotin-AuNP biomolecules of 3D and Gr channel FETs at a channel surface area of  $1 \mu\text{m}^2$ . The density of biotin-AuNPs indirectly reflects the density at which probe biomolecules are immobilized on the sensing channels.

confirm the effective immobilization of the probe proteins on the surface of  $\text{TiO}_2$ -encapped ZnO NRs at a high density before and after oxygen plasma treatments,<sup>48</sup> biotin–streptavidin complexes were used as a test of protein interactions. For this purpose, streptavidin was first immobilized as a probe protein on  $\text{TiO}_2$ -encapped ZnO NRs using the primary amine group in the protein, and the ZnO NRs were incubated with the biotin-AuNP solution for 30 min. After the binding of streptavidin molecules and biotin-AuNPs, the  $\text{TiO}_2$ -encapped ZnO NRs with and without plasma treatments were characterized by FE-SEM (Fig. 2a and b). Clearly, the density of biotin-AuNPs is much higher after (Fig. 2b) oxygen plasma treatment than before (Fig. 2a), due to the increased density of streptavidin probe molecules immobilized onto the plasma-treated surface. The surface density of AuNPs on  $\text{TiO}_2$ -capped ZnO NRs was  $\sim 10^3 \mu\text{m}^{-2}$ , which is comparable to that on the Gr (inset in Fig. 2b). The calculated density of AuNPs on the surface of the 3D channel for a given channel area of  $1 \mu\text{m}^2$  was higher than that on the surface of the Gr channel by a factor of 32 (Fig. 2c). After efficient functionalization of the  $\text{TiO}_2$ -encapped ZnO NRs by the streptavidin protein was confirmed, immunosensing of the prostate specific antigen/1-antichymotrypsin (PSA-ACT) complex antigen (Ag) as an analyte and the PSA-ACT antibody (Ab) as a probe was carried out. The PSA-ACT complex is widely used as a biomarker for the diagnosis of prostate cancer, because PSA is generated from prostatic tissue. Typically, men without prostate cancer have PSA levels below  $4.0 \text{ ng ml}^{-1}$ , while men with prostate cancer have PSA concentrations above  $20.0 \text{ ng ml}^{-1}$ .<sup>49</sup> Early diagnosis is the best way to reduce patient mortality, and quantitative monitoring of PSA is important to patients. Detection of the PSA-ACT complex antigen (PSA-ACT complex Ag) was carried out by static and kinetic measurements. The PSA-ACT Ab was immobilized in the same way as shown in Fig. S5.† The transfer characteristics before and after immobilizing PSA-ACT Ab probe molecules on 3D and 2D channel FETs are shown in Fig. S6a and S6b,† respectively. Larger decreases in the  $I_{\text{DS}}$  and CNP of 3D channel FET were observed compared to those of the 2D channel FET. These results obtained from the 3D channel FET (Fig. 3) may explain the high sensitivity and the



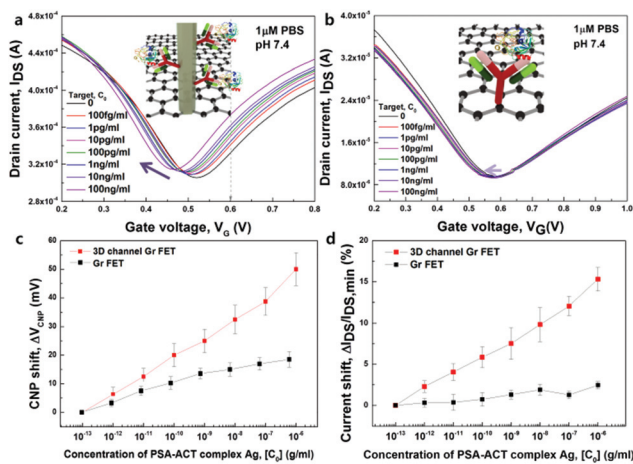


Figure 3

**Fig. 3** Transfer characteristics before and after adding different concentrations of PSA–ACT complex Ag molecules from  $100 \text{ fg ml}^{-1}$  to  $100 \text{ ng ml}^{-1}$  for (a) 3D channel Gr FETs (TiO<sub>2</sub>-encapped ZnO NRs/Gr) and (b) Gr FETs. (c) The shift in charge neutrality point (CNP) as a function of analyte concentration,  $C_0$ . (d) Drain current ( $I_{DS}$ ) of 3D and Gr channel FETs as a function of analyte concentration,  $C_0$ . The CNP was negatively shifted upon increasing the concentration of PSA–ACT complex Ag. Increased  $I_{DS}$  and negative CNP shift ( $\Delta V_{CNP}$ ) with increasing the concentration of PSA–ACT complex Ag molecules were obtained from transfer curves like the ones in (a) and (b) at a gate voltage ( $V_G$ ) of 0.6 V in the linear region. The data in (c) and (d) were averaging the values obtained from five bio-FETs.

wide dynamic range that are attributed to the largely increased density of immobilized Ab probe molecules over the same channel area. Since the charges of proteins are minimally detected by charge screening effects outside the Debye screening length, the analyte solution was prepared by controlling the amount of the PSA–ACT complex Ag in the diluted phosphate buffered saline (PBS) solution.<sup>30,31,50</sup> Accordingly, we carried out immunosensing measurements by diluting analyte molecules in a  $1 \mu\text{M}$  PBS solution, pH 7.4, with a Debye length of  $\sim 70 \text{ nm}$ , which is larger than that of the combined PSA–ACT Ab–Ag ( $\sim 15 \text{ nm}$ ). All measurements were carried out at a  $V_G$  of 1 V to avoid electrolysis by a high gate voltage sweep and after blocking using ethanolamine at 100 mM to prevent interactions between unreacted –CHO groups of glutaraldehyde and the PSA–ACT complex Ag.

The transfer characteristics of 3D and 2D bio-FETs with the analyte concentration,  $C_0$ , of the PSA–ACT complex Ag from  $100 \text{ fg ml}^{-1}$  ( $1.1 \text{ fM}$ ) to  $100 \text{ ng ml}^{-1}$  ( $1.1 \text{ nM}$ ) at  $V_{DS} = 0.1 \text{ V}$ , respectively, are shown in Fig. 3a and b. The transfer curves of both solution-gated bio-FETs were obtained over 10 min while simultaneously adding the analyte solution. For both 3D and 2D bio-FETs, the CNP in the transfer curves ( $V_{CNP}$ ) shifted to negative  $V_G$ ; the current gradually increased with the increase of the PSA–ACT complex Ag concentration. However, the transfer characteristics of the two solution-gated bio-FETs demonstrated a clear difference in the degree of shift of CNP. The  $V_{CNP}$  in both FETs was quantified and plotted as a function of the PSA–ACT complex Ag concentration (Fig. 3c). The shift in

the CNP ( $\Delta V_{CNP}$ ) can be used as a sensitivity parameter due to its superior linearity and the large dynamic range of  $10^7$ . The use of ZnO NRs on the Gr channel significantly increased the  $V_{CNP}$  from  $\sim 2.3 \text{ mV dec}^{-1}$  in the Gr FET to  $\sim 8 \text{ mV dec}^{-1}$  in the 3D FET, indicating that the transduction of biomolecular interactions into the electrical conductance change of the Gr channel intensified using the vertical ZnO NRs. The CNP shift is suggested to occur *via* an electrostatic gating effect, as was previously described in CNT or Si NW bio-FETs.<sup>51</sup> If electrostatic gating effects occur, the CNP would be shifted in the positive direction, as the negative charges of bound PSA–ACT Ag molecules increase at pH 7.4. The PSA–ACT complex Ag is negatively charged above its isoelectric point of 6.8. Negative shifts in CNP with the concentration of target Ag molecules (Fig. 3a) suggest electron doping, which contrasts with hole doping by the electrostatic gating effect. The same phenomenon was observed with the Gr FET (Fig. 3b and c) and has also been reported for rGO FET<sup>30,31</sup> and CVD Gr FET<sup>28,29,52</sup> during protein or DNA interactions. Electron doping in the 3D channel FET is ascribed to the transfer of electrons through the ZnO NRs from biomolecules. Considering the difficulty of direct transfer of biomolecular charges to Gr through ZnO NRs, however, the effects of biomolecular charges on the Fermi level of the n-type ZnO NRs are plausible, because the electron affinities of ZnO NRs ( $\sim -4.4 \text{ eV}$ ) and Gr ( $\sim -4.3 \text{ eV}$ ) are nearly equal. Transfer of electrons from ZnO NRs to the Gr channel increases the Fermi level of Gr, which results in a negative CNP shift. A detailed understanding of the sensing mechanism requires further theoretical and experimental studies. Moreover, the 3D channel FET immobilized with PSA–ACT Ab molecules did not show notable tendencies in the shifts of CNP and  $I_{DS}$  upon adding a carcinoembryonic antigen (CEA) solution with the wide range of concentrations ranging from  $100 \text{ fg ml}^{-1}$  to  $100 \text{ ng ml}^{-1}$  during the reaction time of 10 min (Fig. S7†). The results indicate that PSA–ACT Ab–Ag binding in the 3D channel FET was specific.

The changed  $I_{DS}$  values were plotted against increasing PSA–ACT complex Ag concentrations for the two types of FETs (Fig. 3d). The  $I_{DS}$  change is obtained from the linear region in the transfer curves at  $V_G = 0.6 \text{ V}$ . The  $I_{DS}$  modulation data also show good linearity in the 3D FET compared with that in the 2D FET. Therefore, modulation of  $I_{DS}$  can also be used as a sensitivity factor during immunosensing. The modulation of  $I_{DS}$  ( $I_{DS}/I_{DS,min}$ ) in the 3D FET ( $\sim 2.18\% \text{ dec}^{-1}$ ) was larger than that in the 2D FET ( $\sim 0.3\% \text{ dec}^{-1}$ ) upon increasing the PSA–ACT complex protein Ag. These results support the potential of our developed 3D FET for immunosensing.

Kinetic measurements were employed to detect PSA–ACT complex Ag by stepwise addition of the Ag molecules. Measurements were carried out at fixed  $V_{DS} = 0.1$  and  $V_G = 0.6 \text{ V}$ . There were significant changes in the  $I_{DS}$  of the 3D bio-FET upon adding analyte solutions in low concentration ranges (Fig. 4a), but no significant changes were observed in the  $I_{DS}$  of the Gr channel FET (Fig. S8†). The  $I_{DS}$  in the 3D bio-FET increased in a stepwise fashion when analyte solutions with different concentrations were added. When the same volume of PBS solu-



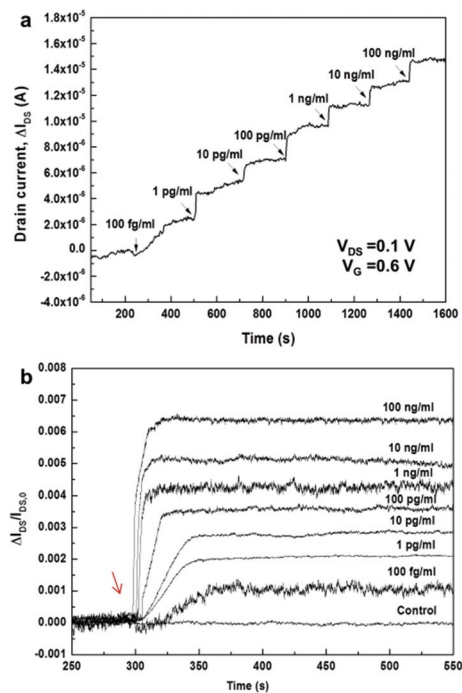


**Fig. 4** (a) Responses of the 3D channel FET upon adding the analyte solutions in different concentrations with a step-wise increase. (b) Time-dependent kinetic responses of 3D channel FETs upon adding the analyte solutions at different concentrations. Each response curve was obtained from different devices. The arrow indicates the time when the antigen solutions are added.

tion without analytes was added into the PDMS well on the 3D FET, the  $I_{DS}$  was not modulated (Fig. S9†). Furthermore, the 3D channel FET was applied to detect the target molecules of PSA-ACT Ag in diluted human serum (0.1%) and the measured data for the concentrations of  $100 \text{ fg ml}^{-1}$ ,  $100 \text{ pg ml}^{-1}$  and  $100 \text{ ng ml}^{-1}$  of the PSA-ACT complex in human serum are shown in Fig. S10a.† The results in Fig. S10a† indicate that the sensor signals in diluted human serum are similar to those of the specific PSA-ACT Ab-Ag binding reaction in diluted PBS solution. However, the sensor responses for the minimum  $100 \text{ fg ml}^{-1}$  concentration of the PSA-ACT complex Ag in 1.0 and 10% diluted human serums are negligible (Fig. S10b†), which is attributed to the charge screening of PSA-ACT Ag molecules in the less diluted human serums having larger ionic strength and, in turn, shorter Debye screening length.

Time-dependent responses of bio-FETs upon adding each target solution with different Ag concentrations from  $100 \text{ fg ml}^{-1}$  to  $100 \text{ ng ml}^{-1}$  were measured and plotted by normalizing the responses as  $\Delta I_{DS}/I_{DS,0}$  for each concentration (Fig. 4b). As the Ag target concentration increased, saturation occurred more rapidly; the increase in the response time matched well with the results of the static measurements at  $V_G = 0.6 \text{ V}$ . At concentrations of  $100 \text{ fg ml}^{-1}$  and  $100 \text{ pg ml}^{-1}$ , for example, the normalized signal was saturated after 64 and 44 s, respectively. Based on the Langmuir model,<sup>53,54</sup> an association constant,  $K_A$ , of  $\sim 16 \text{ pM}^{-1}$  and a  $k_{on}$  of  $\sim 10^6 \text{ M}^{-1} \text{ s}^{-1}$  were

obtained (see Fig. S11†). This value is different from the reported values of, for example,  $\sim 0.9 \text{ nM}^{-1}$  for immunoreactions of PSA mAb and anti-PSA from the surface plasmon resonance biosensor<sup>55</sup> and  $0.4 \text{ pM}^{-1}$  for immunoreactions of PSA mAb and anti-PSA in the SiNW bio-FET.<sup>56</sup> The  $K_A$  value in this work was also smaller than that in the 2D rGO bio-FET ( $\sim 4.2 \text{ nM}^{-1}$ ) reported previously by our group.<sup>30</sup> Even though the reason for this discrepancy for planar 2D and vertically nanostructured 3D surfaces is not clearly understood, it is presumed that the observed discrepancy is possibly attributed to differences in the density, orientation or binding states of immobilized Ab biomolecules on planar 2D and vertical 1D surfaces, resulting in the different binding reactions at equilibrium. A better understanding of the discrepancy may require a further study of the quantitative kinetic analysis in microfluidic systems similarly to the approach by Duan *et al.*<sup>20</sup>

In the well containing bulk target solutions with a relatively large volume ( $400 \mu\text{l}$ ), the mass transport of target molecules occurs by diffusion. While the diffusivity  $D$  of proteins in solution is of the order of  $1\text{--}10 \mu\text{m}^2 \text{ s}^{-1}$ ,<sup>1</sup> the bulk diffusion time of the target proteins towards the ZnO NRs is of the order of  $10^1\text{--}10^2 \text{ min}$ . Indeed, the diffusion time on the 2D rGO channel bio-FET was of the order of tens of minutes.<sup>30</sup> On the other hand, the observed ultrafast response time in the 3D channel FET is presumably attributed to fast binding of the Ag molecules in between ZnO NRs as well as in the vicinity of vertical 1D ZnO NRs. Since the time scale of mass transport of target molecules in between ZnO NRs towards the NR surface is of the order of  $10^{-5} \text{ s}$  considering an average distance between NRs of  $50\text{--}100 \text{ nm}$ , the diffusion of target molecules from the bulk solution only near the top surface of ZnO NRs vertically towards the region of ZnO NRs can be considered. The time scale of vertical mass transport to the bottom of the ZnO NRs was approximated to be of the order of a few seconds after considering the height of the ZnO NRs,  $H$ , of  $\sim 2.5 \mu\text{m}$ . In this situation, the collection rate of target molecules towards the ZnO NRs was approximated by  $J_D = A_c D C_0 / H$ , where the target concentrations at the top and bottom of the ZnO NRs were assumed to be  $C_0$  and zero by neglecting the depletion of target molecules above ZnO NRs. Then, the Damköhler number is given by  $D_a = k_{on} b_m (A_s/A_c) / (D/H)$ . Due to the difficulty of direct measurement of  $b_m$  for the PSA Ab-Ag interactions on the ZnO NRs, the surface density of biotin-Au NPs from streptavidin-biotin interactions,  $\sim 10^3 \mu\text{m}^{-2}$ , was used as the  $b_m$  value on the ZnO sensing surface. This value was lower than the surface density of the PSA Ab probes on rGO, which was indirectly estimated at  $\sim 2 \times 10^5 \mu\text{m}^{-2}$ .<sup>30</sup> The  $D_a$  value was estimated as  $\sim 11$ , which indicates a mass-transport limited regime during Ab-Ag interactions in the 3D channel. We presume that, while the mass transport from the bulk solution towards the ZnO NRs determines the overall binding kinetics, added Ag molecules would be easily captured because of the large number of probe molecules (a large  $b_m A_s$  value) and the short distance in between vertical ZnO NRs and, as a result, faster binding kinetics would lead to a faster electrical response. The range of detection time observed in the present



immunosensing method, close to 1 min at the fM level, is much shorter than the several tens of minutes to hours typically observed for 2D rGO<sup>30</sup> or 1D NW<sup>20</sup> biosensors.

As an alternative reason for the ultrafast response, some charged species near the ZnO NR surface in proximity under the electrical operation of the device might be related to the fast binding kinetics of Ag molecules because negatively charged Ag molecules or other charged particles can be drifted. To investigate the effect of gate electric field on binding kinetics, detection of immunoreactions was measured in the 3D channel FET under no gate biasing ( $V_G = 0$  V). The reaction time of the PSA–ACT complex at 100 fg ml<sup>-1</sup> concentration under no gate biasing was ~70 s (Fig. S12†) similarly to that of the 3D FET under positive gate biasing, which presumably indicates that the drift of charged particles by gate biasing negligibly affects the binding kinetics. The feature of fast response time in the 3D bio-FET could be very important for applications of miniaturized nanobiosensors in diagnostic technology utilizing microfluidic channels where the binding kinetics are limited due to the depletion of target molecules near the 2D sensing surface.<sup>1</sup> Further verification of binding kinetics in microfluidics with mass transport of simultaneous convection and diffusion is needed to elucidate the optimal sensor mechanism and design. The measurement of immunoreactions in the 3D bio-FET indicates the clear advantages of ultrahigh sensitivity, large dynamic range, and ultrafast response time in the field of immunosensing.

## Conclusions

Here, we presented a new sensing platform for a 3D channel bio-FET based on nanostructured materials. We successfully developed a bio-FET with a 3D channel composed of TiO<sub>2</sub>-encapped ZnO NRs vertically grown on CVD Gr for a label-free, ultrasensitive, and ultrarapid electrical biosensor for immunosensing. An ultrathin layer of TiO<sub>2</sub> solved the problem of chemical instability of ZnO NRs in the electrolyte. The use of a 3D channel dramatically increased the number of probe molecules immobilized on the dense, vertical TiO<sub>2</sub>-encapped ZnO NRs in a given channel area compared to that on the 2D Gr channel. Increased probe molecules in a given channel area resulted in a significant improvement in static measurement sensitivity. The results from the 3D channel bio-FET also indicated an extremely large dynamic range of 10<sup>7</sup> and a sensitivity of 8 mV dec<sup>-1</sup> from CNP shifts. The large sensing surface area and shorter distance between vertically grown ZnO NRs facilitated the binding kinetics of analyte-target protein molecules, resulting in a fast response time of ~64 s at an analyte concentration of 100 fg ml<sup>-1</sup> (~1 fM). More research including reusability of the 3D bio-FET sensor and a detailed kinetic analysis need to be performed for further advancement of 3D channel bio-FETs in the near future. The proposed 3D biosensing platform can be easily extended to the detection of various biomolecules other than proteins and various electrochemical detection schemes including voltammetry, amperometry or

impedimetry. Therefore, the newly developed 3D electrochemical 3D bio-FET platform based on nanostructured materials has great potential to be applied to a variety of biosensing systems including disease diagnostics, environmental monitoring, and food safety.

## Experimental

### Graphene synthesis

SLG was synthesized using the CVD method on a copper foil (0.025 mm, Alfa Aesar). The copper foil was cleaned with acetic acid, placed in the middle of a quartz tube furnace, and heated at 1000 °C under a H<sub>2</sub> gas flow of 40 sccm for 20 min. Subsequently, 20 sccm of CH<sub>4</sub> gas was flowed into the tube in order to grow Gr followed by a mixture of H<sub>2</sub> and CH<sub>4</sub> gases at a 2:1 ratio and a pressure of 300 mTorr for 20 min. The heated copper foil was cooled to room temperature under an H<sub>2</sub> atmosphere.

### Graphene transfer

Synthesized SLG was transferred using a gold layer method that can reduce defects and give a very clean Gr surface. A 25 nm gold layer was deposited on Gr grown on copper foils at a deposition rate of 0.1 Å s<sup>-1</sup> using a thermal evaporator. Gold/graphene was separated from the copper foil with a FeCl<sub>3</sub> copper etchant for 2 h (Alfa Aesar) and then subsequently transferred to an acetone/ethanol-cleaned SiO<sub>2</sub> (300 nm)/Si substrate. The sample was cleaned with three rinses of DI water over a 4 h period. After cleaning, the gold/graphene/SiO<sub>2</sub> was naturally dried and annealed to remove water molecules from the interface graphene between SiO<sub>2</sub> at 180 °C for 1 h. The gold layer was then wet etched using a gold etchant (Alfa Aesar) consisting of KI/I<sub>2</sub> and DI water.

### Fabrication process of a 3D channel FET

A schematic illustration of the device is shown in Fig. S1.† Source and drain electrodes of Cr (5 nm) and Au (45 nm) were deposited onto patterned Gr using a shadow mask *via* an e-beam evaporator (Fig. S1a and S1b†). The entire device was covered with an Al<sub>2</sub>O<sub>3</sub> layer of 10 nm as a buffer *via* ALD (Fig. S1c†), and the active area was patterned for active area opening through positive PR photolithography. Using phosphoric acid (~85 wt%, Sigma-Aldrich), the Al<sub>2</sub>O<sub>3</sub> on the Gr surface was etched at 45 °C for 90 s and immediately washed with DI water (Fig. S1d†). The Al<sub>2</sub>O<sub>3</sub> layer was used as a buffer layer to prevent direct contact with various polymers during the photolithographic process and to reduce the leakage current of the device in an aqueous environment. Acetone at 40 °C for 30 min was used to remove positive PR (Fig. S1e†).

### ZnO NR growth and capping by TiO<sub>2</sub>

The solution growth method has been widely used to grow ZnO NRs because of its low temperature growth, size control, and low cost. A dispersion solution of 10 wt% amine-modified ZnO (NPs) in water was dropped onto the graphene surface as



a seed and allowed to dry for 10 min (Fig. S1f†). Subsequently, ZnO NPs were washed using DI water and were immersed in a mixture of hexamethylenetetramine (25 mM, HMTA, C<sub>6</sub>H<sub>12</sub>N<sub>4</sub>) and zinc nitrate hexahydrate (25 mM, Zn(NO<sub>3</sub>)<sub>2</sub>·6H<sub>2</sub>O) in water at 90 °C for 3 h. Grown ZnO NRs were rinsed with DI water and heated at 200 °C for 1 h (Fig. S1g†). The ZnO NRs grown on Gr as an active layer were capped with an ultrathin 1 nm TiO<sub>2</sub> layer using ALD.

### FET encapsulation

All areas except for the channel and electrode pad (contact region for probing) of the 3D channel and Gr FETs were encapsulated using SU-8 negative PR as follows: (1) the device was coated with SU-8 using a spin coater at an optimized spinning speed and time, (2) the fully coated SU-8 device was soft-baked at 95 °C for 3 min, (3) SU-8 was exposed to UV light to make the encapsulation pattern, (4) the exposed device was baked once more at 95 °C for 2 min (post exposure bake), and (5) a development process was carried out in an SU-8 developer for 90 s (Fig. S1h†). To contain the physiological solution, a PDMS well (diameter of 8 mm) was attached onto the device (Fig. S1i†).

### Functionalization of probe biomolecules

(1) The 3D channel FET: To produce hydroxyl groups on the surface of the 3D channel, oxygen plasma treatment was carried out in a microwave plasma reactor. ATPES of 2.5% in ethanol was poured on the channel region at room temperature (RT) for 2 h; it was subsequently rinsed with ethanol and dried using nitrogen gas. To activate amine group-terminated APTES, the device was heated at 150 °C for 20 min. Activated amine groups were reacted with 2.5% GA in a PBS solution at RT for 2 h, and the device was washed using PBS and DI water in sequence. To immobilize streptavidin (Sigma-Aldrich) or PSA-ACT complex Ab molecules (Fitzgerald) onto the surface of the 3D channel, the device was incubated with 100 μl of probe (100 μl ml<sup>-1</sup>) in PBS overnight. After incubation, the channel region was rinsed with PBS.

(2) Gr channel FET: The Gr surface was treated with 1-pyrenebutanoic acid and 10 mM succinimidyl ester (PBSE) in dimethylformamide (DMF) at RT for 2 h in a dark environment. After treatment, the sample was washed to remove unstacked PBSE molecules using DMF and DI water. Immobilization of probe molecules utilized the same process as the 3D channel FET.

### Measurements

Functionalized 3D and Gr channel FETs were used to detect PSA-ACT complex Ag molecules (Fitzgerald). The binding of functionalized streptavidin with biotin-grafted gold nanoparticles (biotin-AuNPs) (Cytodiagnosics) was confirmed by addition of PBS containing 100 nM biotin-AuNPs. For electrical detection of immunoreactions, the 3D and Gr channel FETs with PDMS were placed on the sample holder with the probe tips. During measurements, PBS solutions with different concentrations of PSA-ACT complex Ag molecules (Fitzgerald)

were added into the PDMS well, and transfer characteristics were obtained using a semiconductor parameter analyzer (HP4145B).

## Acknowledgements

This research was supported by the Basic Science Research Program (2013R1A2A1A01015232) through the National Research Foundation (NRF) funded by the Ministry of Science, ICT, & Future Planning, South Korea.

## Notes and references

- 1 T. M. Squires, R. J. Messinger and S. R. Manalis, *Nat. Biotechnol.*, 2008, **26**, 417.
- 2 P. Yager, G. J. Domingo and J. Gerdes, *Annu. Rev. Biomed. Eng.*, 2008, **10**, 107.
- 3 D. Mark, S. Haeberle, G. Roth, F. V. Stetten and R. Zengerle, *Chem. Soc. Rev.*, 2010, **39**, 1153.
- 4 V. Gubala, L. F. Harris, A. J. Ricco, M. X. Tan and D. E. Williams, *Anal. Chem.*, 2012, **84**, 487.
- 5 Y. Wan, Y. Su, X. Zhu, G. Liu and C. Fan, *Biosens. Bioelectron.*, 2013, **47**, 1.
- 6 F. Patolsky, B. P. Timko, G. Zheng and C. M. Lieber, *MRS Bull.*, 2007, **32**, 142.
- 7 J. F. Rusling, G. Sotzing and F. Papadimitrakopoulou, *Bioelectrochemistry*, 2009, **76**, 189.
- 8 D. Wei, M. J. A. Bailey, P. Andrew and T. Ryhänen, *Lab Chip*, 2009, **9**, 2123.
- 9 W. Yang, K. R. Ratinac, S. P. Ringer, P. Thordarson, J. J. Gooding and F. Braet, *Angew. Chem., Int. Ed.*, 2010, **49**, 2114.
- 10 I. M. Feigel, H. Vedala and A. Star, *J. Mater. Chem.*, 2011, **21**, 8940.
- 11 R. Stine, S. P. Mulvaney, J. T. Robinson, C. R. Tamanaha and P. E. Sheehan, *Anal. Chem.*, 2012, **85**, 509.
- 12 S. Liu and X. Guo, *NPG Asia Mater.*, 2012, **4**, e23.
- 13 S. Wu, Q. He, C. Tan, Y. Wang and H. Zhang, *Small*, 2013, **9**, 1160.
- 14 B.-R. Li, C.-C. Chen, U. R. Kumar and Y.-T. Chen, *Analyst*, 2014, **139**, 1589.
- 15 F. Yan, M. Zhang and J. Li, *Adv. Healthcare Mater.*, 2014, **3**, 313.
- 16 B. Zhan, C. Li, J. Yang, G. Jenkins, W. Huang and X. Dong, *Small*, 2014, **10**, 4042.
- 17 J. L. Arlett, E. B. Myers and M. L. Roukes, *Nat. Nanotechnol.*, 2011, **6**, 203.
- 18 F. Patolsky, B. P. Timko, G. Yu, Y. Fang, A. B. Greytak, G. Zheng and C. M. Lieber, *Science*, 2006, **313**, 1100.
- 19 K.-I. Chen, B.-R. Li and Y.-T. Chen, *Nano Today*, 2011, **6**, 131.
- 20 X. Duan, Y. Li, N. K. Rajan, D. A. Routenberg, Y. Modis and M. A. Reed, *Nat. Nanotechnol.*, 2012, **7**, 401.



- 21 P. R. Nair and M. A. Alam, *Appl. Phys. Lett.*, 2006, **88**, 233120.
- 22 P. E. Sheehan and L. J. Whitman, *Nano Lett.*, 2005, **5**, 803.
- 23 G. Zheng, F. Patolsky, Y. Cui, W. U. Wang and C. M. Lieber, *Nat. Biotechnol.*, 2005, **23**, 1294.
- 24 Y. Cui, Q. Wei, H. Park and C. M. Lieber, *Science*, 2001, **293**, 1289.
- 25 R. J. Chen, S. Bangsaruntip, K. A. Drouvalakis, N. W. S. Kam, M. Shim, Y. Li, W. Kim, P. J. Utz and H. Dai, *Proc. Natl. Acad. Sci. U. S. A.*, 2013, **100**, 4984.
- 26 Y. L. Bunimovich, Y. S. Shin, W.-S. Yeo, M. Amori, G. Kwong and J. R. Heath, *J. Am. Chem. Soc.*, 2006, **128**, 16323.
- 27 G. Zheng, X. P. A. Gao and C. M. Lieber, *Nano Lett.*, 2010, **10**, 3179.
- 28 X. Dong, Y. Shi, W. Huang, P. Chen and L.-J. Li, *Adv. Mater.*, 2010, **22**, 1649.
- 29 J. H. Jung, I. Y. Sohn, D. J. Kim, B. Y. Kim, M. Jang and N. E. Lee, *Carbon*, 2013, **62**, 312.
- 30 D.-J. Kim, I. Y. Sohn, J.-H. Jung, O. J. Yoon, N.-E. Lee and J.-S. Park, *Biosens. Bioelectron.*, 2013, **41**, 621.
- 31 D.-J. Kim, H.-C. Park, I. Y. Sohn, J.-H. Jung, O. J. Yoon, J.-S. Park, M.-Y. Yoon and N.-E. Lee, *Small*, 2013, **9**, 3352.
- 32 D. Sarkar, W. Liu, X. Xie, A. C. Anselmo, S. Mitragotri and K. Banerjee, *ACS Nano*, 2014, **8**, 3992.
- 33 L. Wang, Y. Wang, J. I. Wong, T. Palacios, J. Kong and H. Y. Yang, *Small*, 2014, **10**, 1101.
- 34 V. Q. Dang, D.-I. Kim, T. D. Le, B.-Y. Kim, B.-U. Hwang, M. Jang, K.-S. Shin, S.-W. Kim and N.-E. Lee, *Nanoscale*, 2014, **6**, 15144.
- 35 M. Jang, T. Q. Trung, J.-H. Jung, B.-Y. Kim and N.-E. Lee, *Phys. Chem. Chem. Phys.*, 2014, **16**, 4098.
- 36 W. Choi, K.-S. Shin, H. Lee, D. Choi, K. Kim, H.-J. Shin, S.-M. Yoon, J.-Y. Choi and S.-W. Kim, *Nano Res.*, 2011, **4**, 440.
- 37 M. Guo, P. Diao and S. Cai, *J. Solid State Chem.*, 2005, **178**, 1864–1873.
- 38 J. O. Hwang, D. H. Lee, J. Y. Kim, T. H. Han, B. H. Kim, M. Park, K. No and S. O. Kim, *J. Mater. Chem.*, 2011, **21**, 3432.
- 39 B. Liu and H. C. Zeng, *J. Am. Chem. Soc.*, 2003, **125**, 4430.
- 40 D. Polsongkram, P. Chamninok, S. Pukird, L. Chow, O. Lupan, G. Chai, H. Khallaf, S. Park and A. Schulte, *Phys. B (Amsterdam, Neth.)*, 2008, **403**, 3713.
- 41 J. Zhou, N. Xu and Z. L. Wang, *Adv. Mater.*, 2006, **18**, 2432.
- 42 M. Liu, C.-Y. Nam, C. T. Black, J. Kamcev and L. Zhang, *J. Phys. Chem. C*, 2013, **117**, 13396.
- 43 I. Heller, S. Chatoor, J. Männik, M. A. G. Zevenbergen, C. Dekker and S. G. Lemay, *J. Am. Chem. Soc.*, 2010, **132**, 17149.
- 44 E. Uesugi, H. Goto, R. Eguchi, A. Fujiwara and Y. Kubozono, *Sci. Rep.*, 2013, **3**, 1595.
- 45 F. Chen, J. Xia, D. K. Ferry and N. Tao, *Nano Lett.*, 2009, **9**, 2571.
- 46 F. Chen, Q. Qing, J. Xia, J. Li and N. Tao, *J. Am. Chem. Soc.*, 2009, **131**, 9908.
- 47 A. B. Artyukhin, M. Stadermann, R. W. Friddle, P. Stroeve, O. Bakajin and A. Noy, *Nano Lett.*, 2006, **6**, 2080.
- 48 W.-J. Kim, S. Kim, B. S. Lee, A. Kim, C. S. Ah, C. Huh, G. Y. Sung and W. S. Yun, *Langmuir*, 2009, **25**, 11692.
- 49 Y.-E. Choi, J.-W. Kwak and J. W. Park, *Sensors*, 2010, **10**, 428.
- 50 R. B. M. Schasfoort, P. Bergveld, R. P. H. Kooyman and J. Greve, *Anal. Chim. Acta*, 1990, **238**, 323.
- 51 I. Heller, A. M. Janssens, J. Männik, E. D. Minot, S. G. Lemay and C. Dekker, *Nano Lett.*, 2007, **8**, 591.
- 52 T. Y. Chen, P. T. K. Loan, C. L. Hsu, Y. H. Lee, J. T.-W. Wang, K. H. Wei, C. T. Lin and L. J. Li, *Biosens. Bioelectron.*, 2013, **41**, 103.
- 53 A. Halperin, A. Buhot and E. B. Zhulina, *J. Phys.: Condens. Matter*, 2006, **18**, S463.
- 54 A. Lin, A. S.-Y. Lee, C.-C. Lin and C.-K. Lee, *Curr. Proteomics*, 2006, **3**, 271.
- 55 P. S. Katsamba, I. Navratilova, M. Calderon-Cacia, L. Fan, K. Thornton, M. Zhu, T. V. Bos, C. Forte, D. Friend, I. Laird-Offringa, G. Tavares, J. Whatley, E. Shi, A. Widom, K. C. Lindquist, S. Klakamp, A. Drake, D. Bohmann, M. Roell, L. Rose, J. Dorocke, B. Roth, B. Luginbuhl and D. G. Myszka, *Anal. Biochem.*, 2006, **352**, 208.
- 56 Y. Cui, W. U. Wang, L. Huynh and C. M. Lieber, [https://web.stanford.edu/group/cui\\_group/papers/PSA.pdf](https://web.stanford.edu/group/cui_group/papers/PSA.pdf).

